

ASTEROIDS

Spacecraft sample collection and subsurface excavation of asteroid (101955) Bennu

D. S. Lauretta^{1*}, C. D. Adam², A. J. Allen³, R.-L. Ballouz¹, O. S. Barnouin⁴, K. J. Becker¹, T. Becker¹, C. A. Bennett¹, E. B. Bierhaus⁵, B. J. Bos⁶, R. D. Burns⁶, H. Campins³, Y. Cho⁷, P. R. Christensen⁸, E. C. A. Church⁵, B. E. Clark⁹, H. C. Connolly Jr.^{10,1}, M. G. Daly¹¹, D. N. DellaGiustina¹, C. Y. Drouet d'Aubigny¹, J. P. Emery¹², H. L. Enos¹, S. Freund Kasper⁵, J. B. Garvin⁶, K. Getzandanner⁶, D. R. Golish¹, V. E. Hamilton¹³, C. W. Hergenrother^{1†}, H. H. Kaplan⁶, L. P. Keller¹⁴, E. J. Lessac-Chenen², A. J. Liounis⁶, H. Ma⁵, L. K. McCarthy², B. D. Miller⁵, M. C. Moreau², T. Morota⁷, D. S. Nelson², J. O. Nolau³, R. Olds⁵, M. Pajola¹⁵, J. Y. Pelgrift², A. T. Polit¹, M. A. Ravine¹⁶, D. C. Reuter⁶, B. Rizk¹, B. Rozitis¹⁷, A. J. Ryan¹, E. M. Sahr², N. Sakatani¹⁸, J. A. Seabrook¹¹, S. H. Selznick^{1†}, M. A. Skeen⁵, A. A. Simon⁶, S. Sugita⁷, K. J. Walsh¹³, M. M. Westermann¹, C. W. V. Wolner¹, K. Yumoto⁷

Carbonaceous asteroids, such as (101955) Bennu, preserve material from the early Solar System, including volatile compounds and organic molecules. We report spacecraft imaging and spectral data collected during and after retrieval of a sample from Bennu's surface. The sampling event mobilized rocks and dust into a debris plume, excavating a 9-meter-long elliptical crater. This exposed material is darker, spectrally redder, and more abundant in fine particulates than the original surface. The bulk density of the displaced subsurface material was 500 to 700 kilograms per cubic meter, which is about half that of the whole asteroid. Particulates that landed on instrument optics spectrally resemble aqueously altered carbonaceous meteorites. The spacecraft stored 250 ± 101 grams of material, which will be delivered to Earth in 2023.

Carbonaceous asteroids contain materials that are billions of years old and preserve a record of the earliest stages of Solar System evolution (1). Hydrated minerals and organic compounds in carbonaceous chondrite meteorites—which are thought to be fragments of these asteroids—indicate that they may have transported water and prebiotic organic molecules to Earth (2). However, meteorites must survive atmospheric entry, are exposed to terrestrial contamination, and lack geologic context. The Origins, Spectral Interpretation, Resource Identification, and Security–Regolith Explorer (OSIRIS-REx) mission has a primary goal to collect a pristine sample of surface material, from a well-characterized carbonaceous asteroid, and return it to Earth (3, 4).

OSIRIS-REx spent about 2 years surveying (101955) Bennu, a ~500-m-diameter carbonaceous rubble-pile asteroid [for example, (4–6)]. The microgravity environment (7) and unexpectedly rough terrain (5) posed challenges for collecting a sample (4). Nevertheless, after global observations of the surface, a site nicknamed Nightingale was chosen for sampling (4, 8). We describe the sample collection process and its results.

Site of sample collection

Nightingale is situated within the 20-m-diameter Hokioi crater [center coordinates of about 56° , 43° (9)] (Fig. 1A). This site was selected on the basis of spacecraft navigation and safety considerations (4, 10) and an expected higher abundance—relative to the generally boulder-dominated asteroid (5)—of surface particles <2 cm in diameter (11), the size class that is ingestible by the spacecraft's Touch-and-Go Sample Acquisition Mechanism (TAGSAM) (fig. S1) (9). Spectroscopic observations indicated that minerals present at Nightingale include hydrated phyllosilicates (6, 12, 13), the iron oxide magnetite (5, 12, 14), organic molecules (6, 15, 16), and carbonates (6, 17). In panchromatic images, Nightingale exhibits a salt-and-pepper appearance (Fig. 1B), suggesting that Bennu's two primary lithologies—dark with low thermal inertia and brighter with higher thermal inertia (14, 18)—might both be sampled. Hokioi crater is spectrally redder than the average surface of Bennu and thus is thought to be among the youngest features on the surface (14). The crater's midlatitude location limits the peak temperatures it experiences to ~ 360 K (versus

~ 390 K at Bennu's equator) (19), reducing the thermal processing of material there (20).

Sample collection operations and initial surface response

On 20 October 2020, the spacecraft left orbit and descended toward the surface of Bennu for sample collection, guided by autonomous optical navigation (fig. S2) (9). TAGSAM (fig. S1), which comprises a circular sample collection device connected to the spacecraft by a pogo stick-like arm, briefly contacted the asteroid before the spacecraft's back-away thrusters fired (fig. S2)—hence, the moniker Touch-and-Go (TAG) for the sampling maneuver. We investigated the sampling event using data acquired by the SamCam imager, which is part of the OSIRIS-REx Camera Suite (OCAMS); the NavCam 2 imager, which is part of the Touch-and-Go Camera System (TAGCAMS); and the spacecraft's inertial measurement unit (IMU) (9).

Contact and immediate disturbance

TAGSAM contacted the surface at latitude 55.8993° , longitude 41.8412° , with a downward velocity of 10.05 ± 0.004 cm s $^{-1}$ (fig. S3), within 73 cm of the targeted location (9). Camera and IMU data indicate an initial surface contact force of between 10 and 15 N (21). One second after contact, TAGSAM released a jet of nitrogen gas to fluidize unconsolidated surface material and guide it into the collection chamber. About 6 s after contact, the spacecraft retained a downward velocity of ~ 4 cm s $^{-1}$. We attribute the velocity change of 6 cm s $^{-1}$ to TAGSAM gas release. The spacecraft then fired eight of its 4.5-N thrusters, initiating the back-away maneuver. Three seconds of thruster firing arrested the residual downward velocity, then the spacecraft began to retreat from Bennu. By then, TAGSAM had penetrated 48.8 cm into the subsurface. The thrusters fired for a total of 25.7 s, with TAGSAM rising above the original surface height 16.6 s after initial contact. The spacecraft then drifted away from Bennu on a hyperbolic trajectory, at about 30 cm s $^{-1}$.

The surface of Bennu responded to contact as a compliant, viscous fluid, providing minimal resistance to the downward motion of the spacecraft (fig. S4 and movie S1) (21). This response is consistent with simulations of TAGSAM interacting with regolith (unconsolidated rocks and dust) that has near-zero interparticle cohesion (21–23) and low-gravity experiments in which loose material is easily mobilized (24).

Images collected by SamCam 0.8 \pm 0.1 s after contact (0.32 s before gas firing) showed evidence of surface disturbance in all directions around TAGSAM (Fig. 1, C and D). We interpret fig. S5 and movie S2 as showing TAGSAM partially disrupting a ~20-cm-long

¹Lunar and Planetary Laboratory, University of Arizona, Tucson, AZ, USA. ²KinetX, Simi Valley, CA, USA.

³Department of Physics, University of Central Florida, Orlando, FL, USA. ⁴The Johns Hopkins University Applied Physics Laboratory, Laurel, MD, USA. ⁵Lockheed Martin Space, Littleton, CO, USA. ⁶Goddard Space Flight Center, Greenbelt, MD, USA. ⁷Department of Earth and Planetary Environmental Science, University of Tokyo, Tokyo, Japan. ⁸School of Earth and Space Exploration, Arizona State University, Tempe, AZ, USA. ⁹Department of Physics and Astronomy, Ithaca College, Ithaca, NY, USA. ¹⁰Department of Geology, Rowan University, Glassboro, NJ, USA.

¹¹Department of Earth and Space Science and Engineering, York University, Toronto, ON, Canada. ¹²Department of Astronomy and Planetary Science, Northern Arizona University, Flagstaff, AZ, USA. ¹³Southwest Research Institute, Boulder, CO, USA. ¹⁴Johnson Space Center, Houston, TX, USA. ¹⁵Astronomical Observatory of Padova, Italian National Institute for Astrophysics (INAF), Padova, Italy. ¹⁶Malin Space Science Systems, San Diego, CA, USA.

¹⁷School of Physical Sciences, Open University, Milton Keynes, UK. ¹⁸Department of Physics, Rikkyo University, Tokyo, Japan.

*Corresponding author. Email: lauretta@arizona.edu

†Present address: Ascending Node Technologies, Tucson, AZ, USA.

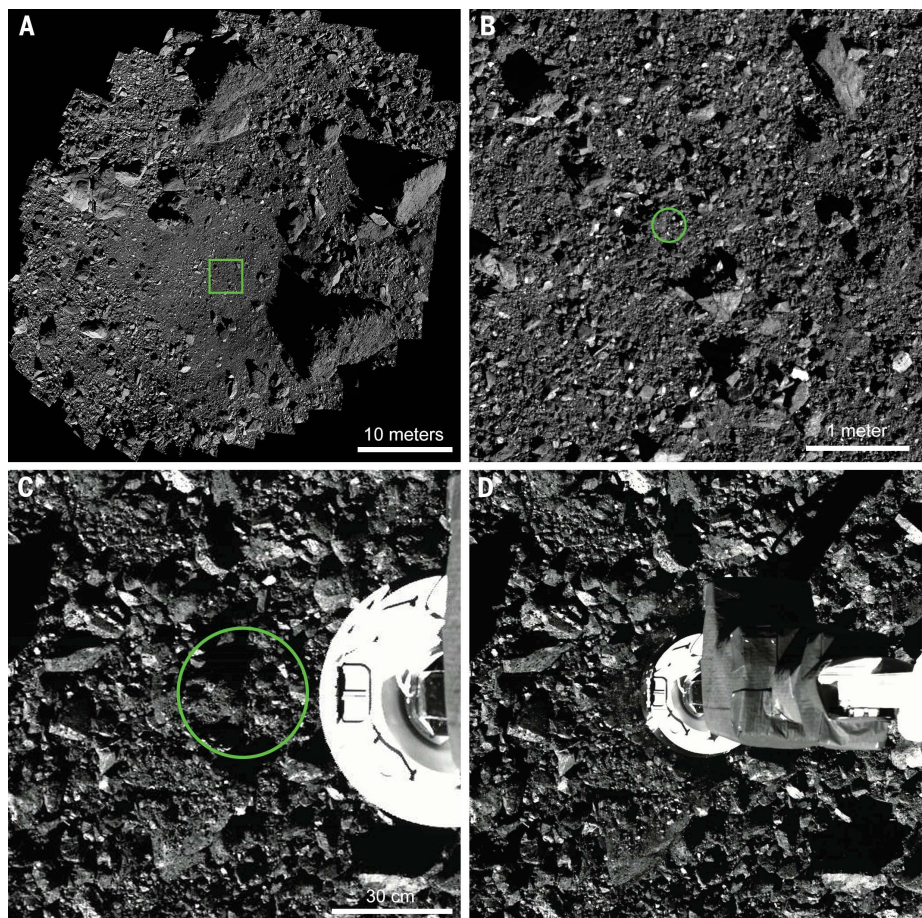


Fig. 1. The Nightingale sample site. (A) Hokioi crater, in a mosaic of images taken by the OCAMS PolyCam imager on 3 March 2020 with a pixel scale of 4 mm. The box indicates the area shown in (B). (B) PolyCam image taken 3 March 2020 with a pixel scale of 0.3 cm, showing a close-up of Hokioi crater. The green circle has a diameter of 32 cm, the same size as TAGSAM, indicating where surface contact occurred. (C) SamCam image of the TAGSAM contact point collected on 20 October 2020, 38 s before surface contact. The green circle is the same as in (B). The image has been cropped to show the same field of view as in (D). (D) SamCam image of TAGSAM contacting Bennu, collected 0.8 s after the first indication of surface interaction from the IMU, 0.32 s before gas bottle firing. Bennu north (+z) is up in all images.

Downloaded from https://www.science.org at University Van Amsterdam on April 13, 2025

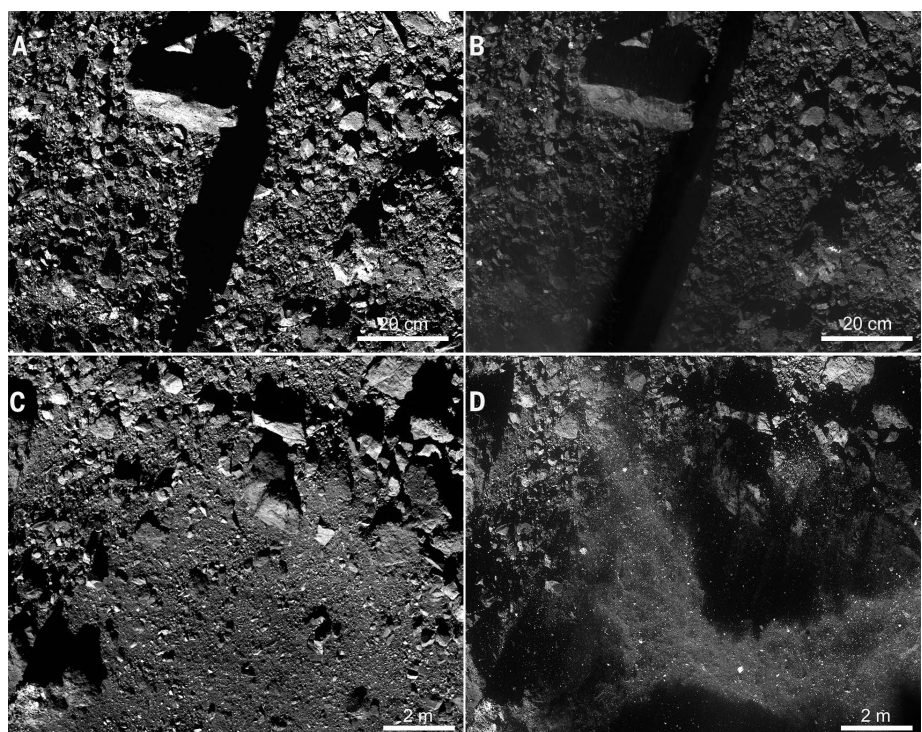


Fig. 2. Dust and debris mobilized by sampling. (A) NavCam 2 image taken immediately before surface contact, at 21:49:49 UTC on 20 October 2020. The shadow of the TAGSAM arm runs through the middle of the image. Pixel scale is 1 mm. (B) Post-contact NavCam 2 image taken at 21:49:50 UTC, with the same field of view as in (A), showing a cloud of submillimeter dust emanating from the TAGSAM contact point (below the field of view). Pixel scale is 1 mm. (C) Pre-contact, high-altitude NavCam2 image taken at 21:42:41 UTC. The TAGSAM contact point is out of the field of view, west of the scene. The image has been cropped to show a similar field of view as in (D). Pixel scale is 15 mm. (D) Post-contact, high-altitude NavCam 2 image taken at 21:51:13 UTC, showing the lofted debris plume. Pixel scale is 9 mm.

boulder near the eastern edge of its contact point. Another boulder, 40 cm long and to the southeast of TAGSAM, responded like a rigid plate, tilting up and launching small particles perched on its surface (fig. S6 and movie S3). These different responses support the inference (from remote sensing) that Bennu's boulders have a range of strengths (18, 25).

Mobilization of dust

Comparing the NavCam 2 image acquired right before surface contact (Fig. 2A) to the image taken 0.1 s after gas release (Fig. 2B) shows a cloud of unresolved fine particulates emanating from the contact point. We used the NavCam 2

images in Fig. 2, A and B, to constrain the mass and particle sizes of this dust cloud. We measured the optical depth of the dust component and integrated over distance from the center of the outflow. The reduction in brightness between the two images constrains the optical model, which indicates average opacity of 0.47, generated by submillimeter particles (9).

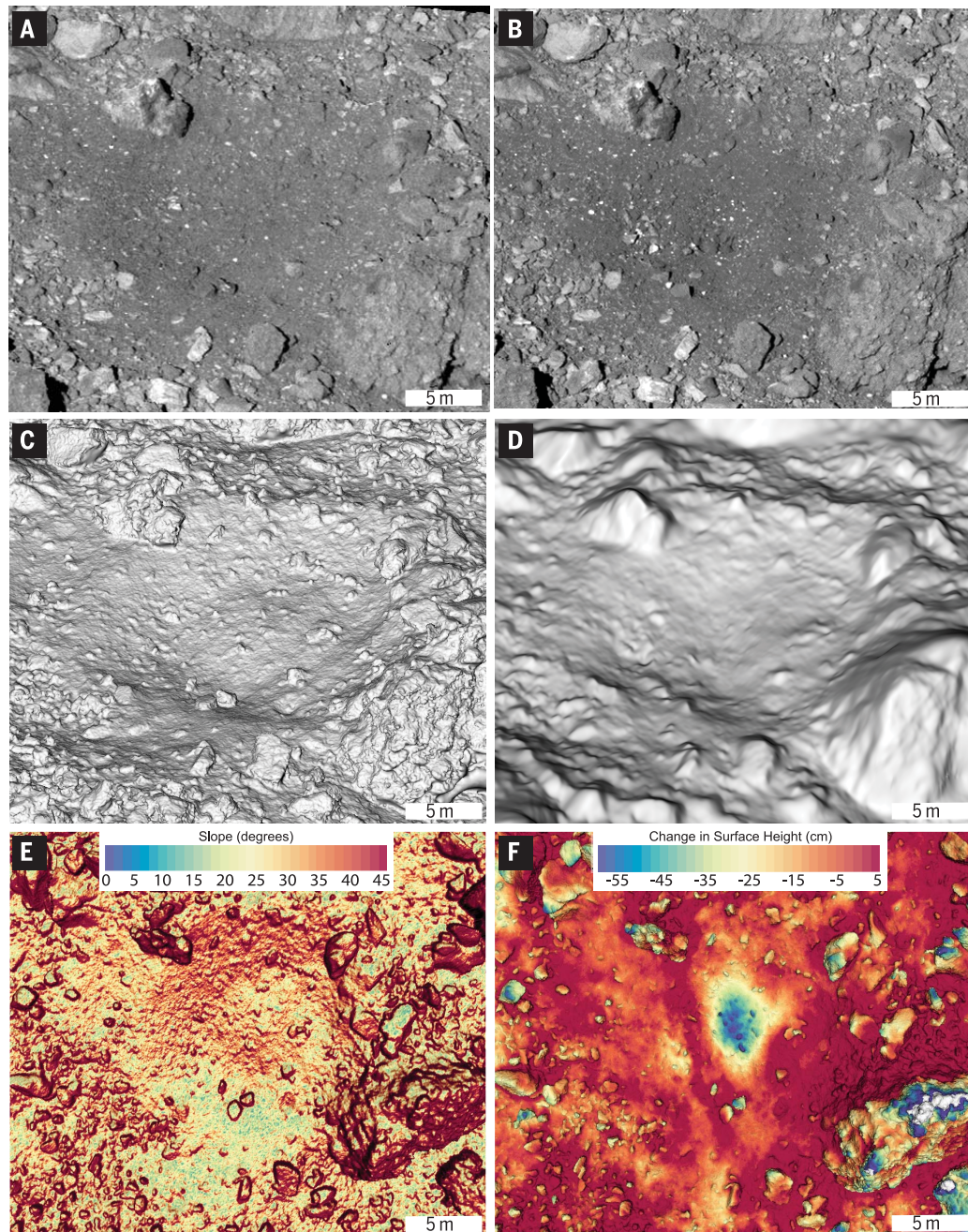
We combined the opacity measurement with an estimated particle size frequency distribution (PSFD) with a maximum size of 3 mm (9), chosen on the basis of the cumulative PSFD from other populations of particles observed at Bennu (11, 26–28) and a theoretical distribution (9). We derived a dust mass of 1.8 ($-1.1/+1.2$) kg.

Assuming a particle density similar to that of carbonaceous chondrites (2000 kg m^{-3}), this mass is equivalent to a dust layer 3.2 ($-2.2/+3.2$) mm thick spread over a 60-cm-diameter circle (twice the diameter of TAGSAM). Previous studies had indicated little to no dust on Bennu's surface, with layer thicknesses tens of micrometers or less (13, 18). Therefore, the subsurface must contain dust that was blown to the surface by the gas release.

Debris plume

Images collected during back-away show a high-opacity debris plume with a large spatial extent, smooth texture (relative to the unperturbed

Fig. 3. Changes in surface appearance and topography after sampling. (A) Pre-sampling image collected on 7 March 2019. (B) Post-sampling image collected on 7 April 2021 (final flyby). These images have a pixel scale of about 5 cm. (C) Pre-sampling DTM based on OLA data, with a ground sample distance of 5 cm. (D) Post-sampling DTM constructed by using stereophotoclinometry (9), with a ground sample distance of 5 cm. The change in topography between (C) and (D) is real, whereas different surface textures in (C) and (D) are due to the different DTM construction methods. (E) Pre-sampling slope map, based on the OLA DTM and calculated surface accelerations (7). (F) Difference in height between the pre- and post-sampling DTMs (9). The deformation near the center is the TAG crater. All DTMs are viewed from an angle of $\sim 68^\circ$, and Bennu north (+z) is up in all images.



surface), and well-defined shadows (Fig. 2, C and D, and fig. S7). Quantitative image analyses (9) indicate that this optically dense, lofted debris plume had a vertical and lateral velocity distinct from the asteroid surface. The morphology of the plume was due to a combination of subsurface excavation by TAGSAM gas release and pressure from the thruster exhaust. The thruster exhaust modified the debris plume, arresting the lateral velocity of finer particulates while permitting larger boulders to continue their eastward motion, indicated by shadows on a flat, bright boulder (movie S4). There was a steep gradient in dynamic pressure surrounding the thruster plumes, causing a range of effects, from total redirection of all particles to only affecting small particulates.

NavCam 2 images show an object in the plume colliding with a stationary rock on the surface, while a nearby tumbling rock spins almost in place, relative to Bennu (movies S4 and S5). The impact occurs at $\sim 10 \text{ cm s}^{-1}$, breaking the impactor apart and changing its direction, before it disappears into the heavily shadowed region. PolyCam images collected during a later flyby (9) show that a 1.25-m boulder, which was directly under one set of thrusters, was transported 12 m to well outside Hokioi crater (fig. S8 and movie S6).

These observations support our interpretation that TAGSAM partially disrupted a boulder at the contact point. We suggest that some

of the fine material in the debris plume was produced during the sampling event through the destruction of initially larger rocks. We measured the size of moving particles in the debris plume in consecutive NavCam 2 images (9). We found a power-law PSFD from 2.5 to 30 cm with an index of -3.3 ± 0.4 , whereas previous high-resolution measurements of Nightingale found an index of -2.3 ± 0.3 (fig. S9 and table S1). This difference indicates that the material mobilized by sampling contained a higher proportion of fine particulates than the precontact surface.

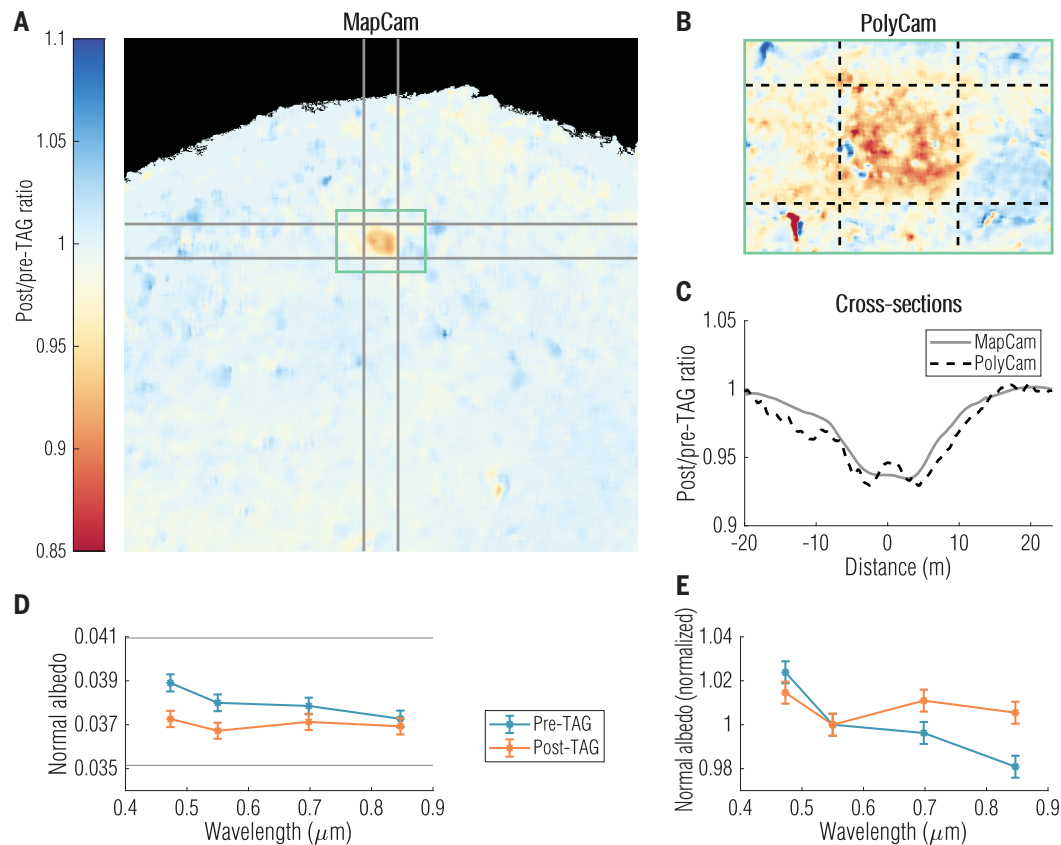
Properties of the subsurface exposed by sampling

The spacecraft, which had been drifting away from the asteroid since sample collection, returned to Bennu on 7 April 2021 for a final flyby to characterize the newly exposed subsurface (fig. S10 and tables S2 and S3). Observations were taken 3.7 km from Bennu in a series of north-south linear scans, optimized for the PolyCam telescopic imager, which obtained images at 5 cm pixel scale (nadir resolution) (9). Observations were also taken by the MapCam multispectral imager at 25 cm pixel scale, the OSIRIS-REx Thermal Emission Spectrometer (OTES) at 28.2 m footprint, and the OSIRIS-REx Visible and InfraRed Spectrometer (OVIRS) at 14.1 m footprint (9).

Crater formed by spacecraft interaction

Comparison of PolyCam images, collected during the global survey of Bennu in 2019 and the final flyby in 2021 (Fig. 3, A and B), shows changes to the Hokioi crater caused by the sampling event. We applied stereophotoclinometry to the final flyby images to construct a digital terrain model (DTM) with 5-cm ground sample distance (Fig. 3D) (9). We registered portions of the images to landmarks exterior to Hokioi crater that were not affected by sampling and compared the results with a previous DTM constructed at the same resolution, using OSIRIS-REx Laser Altimeter (OLA) data taken before sampling (Fig. 3C) (9). We found that the sampling event removed the edge of a preexisting debris apron at the base of the Hokioi crater wall (Fig. 3, A and C, and fig. S8) and replaced it with a crater (centered at $55.997^\circ, 44.971^\circ$) with several boulders at its bottom, which we nickname the TAG crater (Fig. 3, B, D, and F; and figs. S8, S11, and S12). This excavated crater is elliptical (9.0 by 6.5 m), with its long axis oriented north to south. Its average lateral dimension is $7.8 \pm 1.8 \text{ m}$, and its depth is $0.68 \pm 0.1 \text{ m}$. The displaced volume is $12.2 \pm 0.9 \text{ m}^3$. It is surrounded by decimeter-scale rocks that were transported by the sampling event into an arc (fig. S8), resembling the stone rings seen around small impact craters elsewhere on Bennu's surface (29).

Fig. 4. Changes in surface optical properties after sampling, measured with OCAMS. (A and B) Reflectance changes in (A) MapCam and (B) PolyCam data before and after sampling (TAG). (C) Plot of reflectance change across Hokioi crater. (D) Absolute reflectance from MapCam color filters. The error bars indicate the 1% relative uncertainty between filters (9). The horizontal gray bars indicate the absolute radiometric uncertainty. (E) The same spectra normalized to $0.55 \mu\text{m}$. The error bars indicate the relative uncertainty of $\pm 0.25\%$ between pre- and post-TAG imaging (9).



The differences between the pre- and post-sampling DTMs indicate that the elliptical shape of the TAG crater arises from two factors. First, the sampling event occurred on a 20° to 30° north-to-south slope, relative to Bennu's gravity vector (Fig. 3E). We infer that a transient crater formed when the gas release led to upslope steepening, in excess of the angle of repose, especially to the north and northwest. This interaction would have led to subsequent mass wasting, producing the elliptical shape and the rock accumulations at the crater center (Fig. 3B and fig. S8). In mass movements on Earth (30) and on asteroids (31), larger blocks can surf on the finer particles of regolith, flowing downslope, and are the last to be buried. Second, the sampling event excavated surface material along the north-south long axis of the TAG crater and along a line running along its short axis from the west-southwest to east-northeast (Fig. 3F and figs. S11 and S12). These shallow trenches of material loss correspond to the orientation of the back-away thrusters, so we conclude that they were produced when the spacecraft pulled away from the surface. We estimate that the thrusters increased the volume of the crater by $\sim 40\%$ (figs. S11 and S12).

Elliptical morphology and accumulation of larger rocks at the crater bottom can occur in low-velocity ($<500 \text{ m s}^{-1}$) impact experiments on a 20° to 25° slope in Earth gravity (32–34). Surface flow due to parallel erosion of the walls of a transient crater can lead to sorting, with coarser pebbles and less dense materials floating to the top, whereas smaller fines are buried below (31). In such flows, large rocks tend to move to the toe of the flow and can be partially buried when they come to a stop at the center of the crater, as more flow follows behind. Depth profiles through the TAG crater indicate removal of up to 20 cm of material over a broad region in the north and north-northeast (fig. S11), along the steepest areas of the Hokioi crater wall. This portion of the wall likely readjusted through surface failure, in response to the formation of the TAG crater.

Physical properties of the subsurface

We applied crater scaling relationships (35–37) and used the known energy of the gas released to assess the physical properties of the rubble in which the TAG crater formed (table S4) (9). As an upper bound, we assumed that the entire 8-m (average diameter) TAG crater is the result of TAGSAM gas release. As a lower

bound, we removed the possible contribution to the crater size from thruster effects, yielding a 5-m average diameter (fig. S12).

For rubble-pile asteroids, intermolecular attraction may result in cohesive forces between particles, with values approximately equal to the gravitational force (23, 38). For both crater sizes considered, however, a nearly cohesionless ($<0.001 \text{ Pa}$) granular material is required (fig. S13, G to I). Even under these conditions, the energy associated with TAGSAM gas release does not reproduce the observed crater if the bulk density of the regolith is equal to that of the global Bennu average [1190 kg m^{-3} (5)]. Instead, the observed crater size indicates a local bulk density of 500 to 700 kg m^{-3} (fig. S13, G to I). This range is consistent with independent results from spacecraft accelerometer data and granular mechanics models (27). This density, combined with the estimated excavation volume, suggests that the sampling event mobilized at least $6000 \pm 650 \text{ kg}$, which is substantially more than predicted (39).

Particle size differences

We counted particles in PolyCam images of the sample site (fig. S14) taken during the final flyby to determine the PSFD of the newly

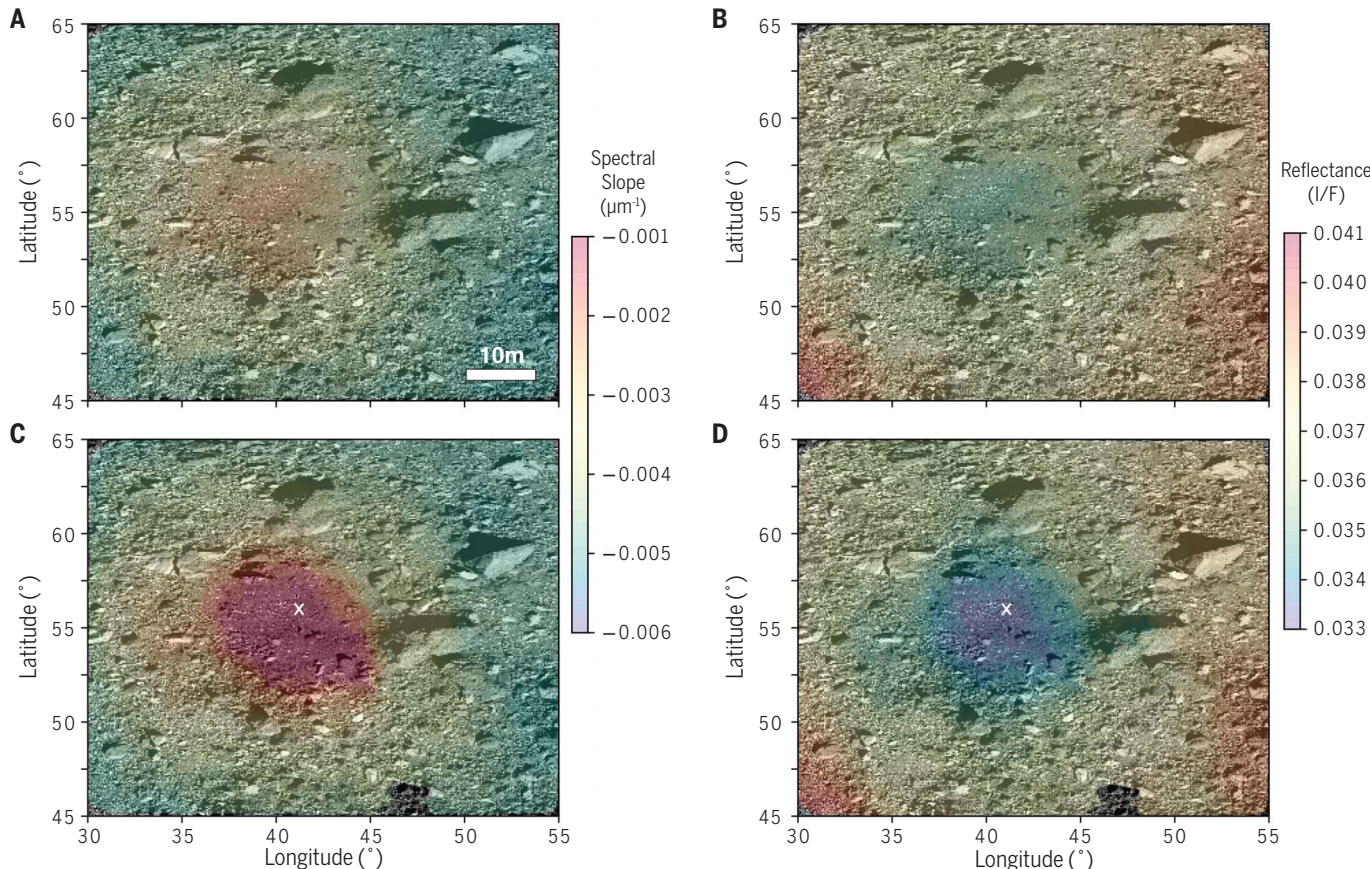


Fig. 5. Changes in surface spectral properties measured with OVIRS. Data collected with OVIRS (color) are overlaid on a pre-sampling PolyCam image of the sample site. (A) Spectral slope from 0.5 to 1 μm before sampling. (B) Reflectance at 0.55 μm before sampling. (C and D) Same as (A) and (B), but after sampling. The sampling location is indicated with the white cross.

exposed subsurface (fig. S9 and table S1) (9). Before sampling, particle counts from PolyCam images of Nightingale, obtained at the same imaging conditions as the final flyby, yielded a PSFD power-law index of -1.9 ± 0.2 (11). The final flyby data have a power-law index of -2.5 ± 0.1 (fig. S9). The sampling event thus decreased the exponent in the power-law distribution of visible particles. The change in PSFD is likely a combination of particle fragmentation from TAG combined with a subsurface reservoir of fine particles (Fig. 2, A and B).

Optical and spectral differences

Post-sampling MapCam and PolyCam data (figs. S15 and S16) (9) show that Nightingale is darker overall, with normal albedo decreased by 5% (Fig. 4, A to C). However, a greater amount of high-reflectance material [relative to the generally dark surface (5, 14, 28)] is visible near the contact point after sampling (Fig. 3, A and B). MapCam color data show that the Nightingale surface became spectrally redder in the wavelength range 0.55 to 0.85 μm and an absorption band near 0.55 μm , which is indicative of magnetite, is deeper than before sampling (Fig. 4, D and E, and table S5) (5).

The post-sampling surface is also spectrally redder and darker in OVIRS spectra (Fig. 5), compared with data collected before sampling (6). The visible–near-infrared spectral slope (0.5 to 1 μm) at the sampling site increased by 58% (figs. S17 and S18 and table S5). Reflectance at 0.55 μm decreased by ~5% relative to previous observations, after accounting for reduced optical throughput (9). These changes do not extend past the edge of Hokioi crater (fig. S18 and table S5). The OVIRS detector was too warm during the post-sampling observations to determine changes at longer wavelengths. Comparison of pre-sampling (13) and post-sampling OTES spectra shows no detectable change in thermal properties of the surface at Nightingale (figs. S19 to S21) (9).

Previous work on color variation across Bennu's surface proposed that the most freshly exposed surfaces are among the reddest and darkest (14); our results support this interpretation. We attribute the spectral changes to the exposure of fresh, organic-rich material (supplementary text).

Properties of the collected sample

In-flight inspection of the sample

SamCam took images of TAGSAM 2 days after sampling (22 October 2020). SamCam and the TAGCAMS imager StowCam acquired further images 8 days after sampling (28 October 2020), just before TAGSAM was stowed in its protective return capsule (9). These images showed that the TAGSAM collection chamber was packed with sample (fig. S22), with the average brightness of the chamber reduced to 1.5% of its pre-sampling value. The images also

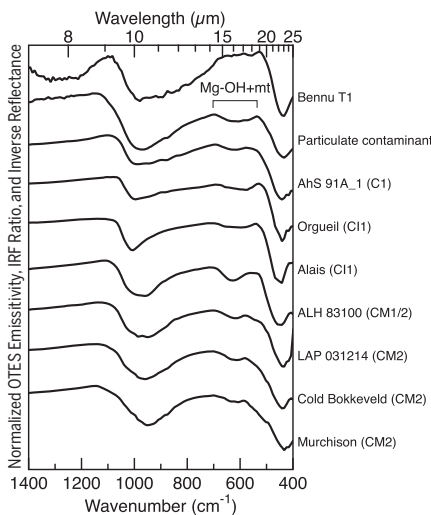


Fig. 6. Spectroscopic comparison of Bennu to carbonaceous chondrite meteorites. From top to bottom, the lines are an example Bennu surface spectrum acquired by OTES before sampling [type T1 (13)]; the spectrum of the contaminating particulates on the instrument mirror after sampling; and spectra of aqueously altered CI and CM chondrites (13), which are proposed Bennu-analog meteorites. Spectra are offset vertically for clarity; the Bennu T1 spectrum is scaled by 300% for comparison of spectral features. The small Mg-OH plus magnetite (mt) absorption from ~ 700 to 535 cm^{-1} (~ 14.3 to $18.7 \mu\text{m}$) in the particulate spectrum was not detectable in Bennu surface observations but is common among the Cls and CMs. IRF, instrument response function.

showed 23 particles, up to 4 mm in diameter, clinging to the TAGSAM contact pads (fig. S23 and table S6). The pattern of specular and diffuse reflection on each pad across different illumination conditions indicates the presence of unresolved particles. More than 260 submillimeter particles adhered directly to other parts of TAGSAM (fig. S23 and table S6). We anticipate that submillimeter dust mobilized by the sampling event (Fig. 2, A and B) is also trapped in the pads.

These images also showed that TAGSAM was overflowing and losing particles (fig. S24). Several pebbles with long axes up to 3 cm were visibly wedged in the chamber mouth, propping open the mylar flap that was intended to prevent material from escaping (fig. S22).

To characterize the sample loss, we tracked 1804 individual particles leaving TAGSAM in the SamCam verification images taken 2 days after sampling (9). During this verification sequence, the TAGSAM wrist motor performed nine different articulations, each imaged by SamCam with multiple exposure times. Each tracked particle was observed in at least three images, allowing their trajectories to be estimated and traced back to TAGSAM, by using methods previously developed to track par-

ticles ejected from Bennu's surface (26, 27, 40). The median estimated range from the camera to the particles at the time of their first observation was 2.4 m, and the median estimated particle velocity was 0.8 cm s^{-1} (fig. S25). We observed the largest number of particles (560, or 31% of all escaping particles observed) leaving just after the first movement of the wrist (fig. S24A). Fewer escaping particles were observed with each successive wrist movement (fig. S24, B to H), until the wrist reversed direction, at which point the number of escaping particles increased (fig. S24I).

We estimated the size and mass of each tracked particle (fig. S25) (9). The escaping particles had a flake-like shape (fig. S26), which is consistent with particles naturally ejected from Bennu (27, 41). Their long dimensions ranged from 0.004 to 23 mm, with a mean of 0.92 mm. We estimate that at least 55 g of material left TAGSAM, with a mean particle mass of 0.03 g and an average mass loss rate of 2.2 g min^{-1} throughout the imaging sequence. The tracked particles are only a fraction of the total particles in the images, which in turn are likely only a fraction of the total particles that escaped. Thus, these results represent a lower bound on the sample mass lost.

Sample mass from momentum transfer analysis

To estimate the mass of the collected sample, the spacecraft was programmed to hold an inertially fixed attitude while the TAGSAM arm moved to determine the exchange of momentum between TAGSAM and the reaction wheels (42). This activity was performed three times: before sampling (zero mass), 2 days after sampling (concurrent with SamCam verification imaging), and 8 days after sampling (concurrent with SamCam and StowCam verification imaging). Analysis of the momentum transfer (42) indicates that at 2 days after sampling, TAGSAM contained $317 \pm 101 \text{ g}$ of sample. This mass is consistent with a prediction of 252 to 575 g (8) based on empirical formulations of TAGSAM performance under the observed sampling conditions. By the next measurement (8 days after sampling), just before sample stowage, the same technique was used to measure a sample mass of $250 \pm 101 \text{ g}$ (42), indicating that TAGSAM lost 67 g in the interim.

Size-frequency distribution of particles on TAGSAM

We measured the diameters of particles on top of TAGSAM in SamCam images during back-away. Even though these particles were removed before sample stowing, we obtained their PSFD as an approximation for that of the captured sample (fig. S9A and table S1) (9). The obtained PSFD follows a power law with an average index of -2.2 ± 0.3 . This value is consistent with the power-law index of -2.3 ± 0.3

measured at Nightingale before sampling (11). However, given the observed friability of Bennu particles, the PSFD of the sample after experiencing atmospheric entry forces upon delivery to Earth in 2023 might not resemble that of either Nightingale or the initially collected sample.

Composition of particulates on instrument optics

The mobilization of a dust cloud and debris plume resulted in the accumulation of particulates on the optics of the OSIRIS-REx science instruments (table S7) (9). After sample collection, OTES was found to have experienced a ~15% decrease in signal, of which only about ~1% can be attributed to fluctuations in the measured instrument temperature. We used this optical contamination to spectrally characterize the particulates (Fig. 6) by taking the ratio of OTES observations of space before and after sampling (9). Because the instrument, and thus the particulates, are hotter than the background space, the contaminant spectrum is analogous to an emission spectrum (43).

This spectrum resembles that of Bennu's surface (12, 13), with features attributed to stretching and bending modes in phyllosilicate minerals (Fig. 6). Absorption bands due to magnetite are deeper than on Bennu's surface. In addition, we observed a compound absorption band centered near 605 cm^{-1} (~16.5 μm), which we attribute to an Mg-OH stretching mode in hydrated Mg-rich phyllosilicates, plus a stretching mode in magnetite (44, 45).

Mg-rich phyllosilicates are diagnostic of high degrees of aqueous alteration (1)—that is, secondary mineralization owing to rock-fluid interactions that took place early in Solar System history, on the precursor bodies of carbonaceous asteroids. Previous analyses of OTES data posited that Bennu's phyllosilicates were Mg-rich (12), but we could not confirm this because the 605 cm^{-1} compound absorption was not detectable and the silicate stretching band was distorted by thin dust deposits (13). Our post-sampling particulate spectrum substantiates the previously published interpretation (12) of Bennu as analogous to the most aqueously altered, chemically primitive (46) carbonaceous meteorites: the CI (Ivuna-type) and CM (Mighei-type) carbonaceous chondrites.

Conclusion

TAGSAM collected a much greater sample than the mission's requirement of 60 g (3, 4), which we attribute to the soft, noncohesive, low-bulk-density surface and upper subsurface (top ~50 cm) of Bennu. Although large particles (a few centimeters) wedged in the TAGSAM flap led to the loss of some collected sample, hundreds of grams were stowed for return to Earth (42). Our observations of dust mobilization and surface changes suggest that the sam-

ple may have different textural properties than the surface and should include material that has undergone different degrees of space weathering (14).

REFERENCES AND NOTES

- D. S. Lauretta, H. Y. McSween, Eds., *Meteorites and the Early Solar System II* (Univ. Arizona Press, 2006).
- C. Chyba, C. Sagan, *Nature* **355**, 125–132 (1992).
- D. S. Lauretta et al., *Space Sci. Rev.* **212**, 925–984 (2017).
- D. S. Lauretta, H. L. Enos, A. T. Polit, H. L. Roper, C. W. V. Wolner, in *Sample Return Missions*, A. Longobardo, Ed. (Elsevier, 2021), pp. 163–194.
- D. S. Lauretta et al., *Nature* **568**, 55–60 (2019).
- A. A. Simon et al., *Science* **370**, eabc3522 (2020).
- D. J. Scheeres et al., *Sci. Adv.* **6**, eabc3350 (2020).
- K. J. Walsh et al., *Space Sci. Rev.* **218**, 20 (2022).
- Materials and methods are available as supplementary materials.
- K. Berry et al., 43rd Annual AAS Guidance, Navigation and Control Conference, Breckenridge, CO, paper AAS 20-088 (2020).
- K. N. Burke et al., *Remote Sens.* **13**, 1315 (2021).
- V. E. Hamilton et al., *Nat. Astron.* **3**, 332–340 (2019).
- V. E. Hamilton et al., *Astron. Astrophys.* **650**, A120 (2021).
- D. N. DellaGiustina et al., *Science* **370**, eabc3660 (2020).
- A. A. Simon et al., *Astron. Astrophys.* **644**, A148 (2020).
- H. H. Kaplan et al., *Astron. Astrophys.* **653**, L1 (2021).
- H. H. Kaplan et al., *Science* **370**, eabc3557 (2020).
- B. Rozitis et al., *Sci. Adv.* **6**, eabc3699 (2020).
- B. Rozitis et al., *J. Geophys. Res. Planets* **125**, e2019JE006323 (2020).
- M. Delbô, P. Michel, *Astrophys. J. Lett.* **728**, L42 (2011).
- K. J. Walsh et al., *Sci. Adv.* 10.1126/sciadv.abm6229 (2022).
- R. Ballouz, "Numerical simulations of granular physics in the solar system," thesis, University of Maryland, College Park, MD, 2017.
- R. Ballouz et al., *Mon. Not. R. Astron. Soc.* **507**, 5087–5105 (2021).
- N. Murdoch et al., *Mon. Not. R. Astron. Soc.* **503**, 3460–3471 (2021).
- R.-L. Ballouz et al., *Nature* **587**, 205–209 (2020).
- D. S. Lauretta et al., *Science* **366**, eaay3544 (2019).
- C. W. Hergenrother et al., *J. Geophys. Res. Planets* **125**, e2020 (2020).
- D. N. DellaGiustina et al., *Nat. Astron.* **3**, 341–351 (2019).
- E. B. Bierhaus et al., *Nat. Geosci.* **15**, 440–446 (2022).
- R. M. Iverson, M. E. Reid, R. G. LaHusen, *Annu. Rev. Earth Planet. Sci.* **25**, 85–138 (1997).
- V. Perera, A. P. Jackson, E. Asphaug, R.-L. Ballouz, *Icarus* **278**, 194–203 (2016).
- J. Aschauer, T. Kenkmann, *Icarus* **290**, 89–95 (2017).
- K. Hayashi, I. Sumita, *Icarus* **291**, 160–175 (2017).
- R. T. Daly et al., in *Proceedings of the 15th Hypervelocity Impact Symposium, Destin, FL, USA* (American Society of Mechanical Engineers, 2019), pp. 237–244.
- K. A. Holsapple, *Annu. Rev. Earth Planet. Sci.* **21**, 333–373 (1993).
- K. R. Housen, K. A. Holsapple, *Icarus* **211**, 856–875 (2011).
- K. R. Housen, R. M. Schmidt, K. A. Holsapple, *J. Geophys. Res.* **88** (B3), 2485–2499 (1983).
- D. C. Richardson, P. Michel, K. J. Walsh, K. W. Flynn, *Planet. Space Sci.* **57**, 183–192 (2009).
- E. B. Bierhaus et al., *Icarus* **355**, 114142 (2021).
- J. Y. Pilgrift et al., *Earth Space Sci.* **7**, e2019EA000938 (2020).
- S. R. Chesley et al., *J. Geophys. Res. Planets* **125**, e2019JE006363 (2020).
- H. Ma, M. Skeen, R. Olds, B. Miller, D. S. Lauretta, arXiv:2109.05561 [astro-ph.EP] (2021).
- S. W. Ruff et al., *J. Geophys. Res.* **111**, E12S18 (2006).
- R. D. Hanna et al., *Icarus* **346**, 113760 (2020).
- M. Ishii, M. Nakahira, T. Yamanaka, *Solid State Commun.* **11**, 209–212 (1972).
- N. Grevesse, M. Asplund, J. Sauval, *Space Sci. Rev.* **130**, 105–114 (2007).
- B. Rizk, C. Drouet d'Aubigny, D. Golish, D. N. DellaGiustina, D. S. Lauretta, NASA Planetary Data System, urn:nasa:pds:orex:ocams, version 10.0 (2019); <https://arcnav.psi.edu/urn:nasa:pds:context:instrument:ocams.orex>.
- C. Bos, Jackman, D.S. Lauretta, NASA Planetary Data System, urn:nasa:pds:orex:tagcams, version 10.0 (2019); <https://arcnav.psi.edu/urn:nasa:pds:context:instrument:tagcams.orex>.
- P. Christensen, V. Hamilton, S. Anwar, G. Mehall, D. S. Lauretta, NASA Planetary Data System, urn:nasa:pds:orex:otes, version 10.0 (2019); <https://arcnav.psi.edu/urn:nasa:pds:context:instrument:otes.orex>.
- D. C. Reuter, A. A. Simon, A. Lunsford, D. S. Lauretta, NASA Planetary Data System, urn:nasa:pds:orex:ovirs, version 10.0 (2019); <https://arcnav.psi.edu/urn:nasa:pds:context:instrument:ovirs.orex>.
- M. Daly, O. Barnouin, R. Espiritu, D. Lauretta, NASA Planetary Data System, urn:nasa:pds:orex:ola, version 3.0 (2019); <https://arcnav.psi.edu/urn:nasa:pds:context:instrument:ola.orex>.

ACKNOWLEDGMENTS

The OSIRIS-REx sample collection event was the culmination of years of effort by hundreds of team members in the face of substantial challenges. We are grateful to all who contributed.

Funding: D.S.L., C.W.V.W., C.D.A., D.S.N., J.Y.P., E.M.S., E.J.L.-C., L.K.M., C.W.H., K.J.W., R.L.B., O.S.B., D.N.D., K.J.B., T.B., C.A.B., D.R.G., C.Y.D'A., B.Ri., B.J.B., J.B.G., M.A.R., R.B., M.C.M., H.C., A.A., J.N., V.E.H., P.R.C., A.A.S., B.E.C., H.H.K., D.C.R., H.L.E., A.T.P., M.M.W., S.H.S., K.G., A.J.L., L.P.K., R.O., H.M., B.D.M., M.A.S., S.F.K., E.C.A.C., A.J.R., J.P.E., and H.C.C. were supported by NASA under contract NNM10AA1C issued through the New Frontiers Program. M.P. was supported by the Italian Space Agency (ASI) under the ASI-INAF agreement 2017-37-H.0. S.S. was supported by the International Network of Planetary Sciences grant from the Japanese Society for Promotion of Science (JSPS) Core-to-Core program. B.Ro. acknowledges funding support from the UK Science and Technology Facilities Council (STFC). M.G.D. and J.A.S. were supported by the Canadian Space Agency. **Author contributions:** D.S.L. led the investigation and compiled, integrated, and interpreted the results, supported by C.W.V.W.; C.D.A. led the investigation of escaping particles from TAGSAM, supported by D.S.N., J.Y.P., E.M.S., E.J.L.-C., and L.K.M.; C.W.H. analyzed the shapes of particles escaping from TAGSAM and supported their photometric analysis. K.J.W. led the evaluation of regolith properties, supported by R.L.B.; O.S.B. led the altimetry investigation of the TAG crater, supported by M.G.D. and J.A.S.; M.G.D. is the instrument scientist for OLA. D.N.D. led the image processing of OCAMS data, supported by K.J.B., T.B., C.A.B., D.R.G., C.Y.D'A., and B.Ri.; C.Y.D'A. and B.Ri. are the OCAMS instrument scientists. E.B.B. is the TAGSAM lead scientist and analyzed the thruster contribution to surface modification. B.J.B. is the TAGCAMS instrument scientist and led the image processing of TAGCAMS data, supported by J.B.G. and M.A.R.; R.B. and M.C.M. are the project managers for the OSIRIS-REx mission. M.P. led the particle size frequency analysis of the final flyby data, supported by H.C., A.A., and J.N.; S.S. performed the particle size frequency analysis of the TAGSAM head and the debris plume, supported by Y.C., T.M., N.S., and K.Y.; V.E.H. led the spectral analysis of OTES data, supported by P.R.C.; P.R.C. and V.E.H. are the OTES instrument scientists. A.A.S. led the spectral analysis of OVIRS data supported by B.E.C., H.H.K., and D.C.R.; D.C.R. and A.A.S. are the OVIRS instrument scientists. H.L.E. led the science operations team, supported by A.T.P., M.M.W., and S.H.S.; K.G. led the flight dynamics and navigation team, supported by C.D.A., D.S.N., J.Y.P., E.M.S., E.J.L.-C., A.J.L., and L.K.M.; L.P.K. led the analysis of the contact pads, supported by B.Ri.; R.O. led the analysis of spacecraft momentum buildup, supported by H.M., B.D.M., and M.A.S.; S.F.K. led the spacecraft operations team. E.C.A.C. was the TAG lead system engineer. B.Ro. led the thermal analysis, supported by A.J.R. and J.P.E.; H.C.C.Jr. is the mission sample scientist and supported interpretation of the collected sample.

Competing interests: The authors declare that they have no competing interests. **Data and materials availability:** Data from the sampling event and/or the final flyby are available in the Planetary Data System at <https://sbn.psi.edu/pds/resource/orex> in the datasets devoted to OCAMS (47), TAGCAMS (48), OTES (49), OVIRS (50), and OLA (51). The IDs of the images, spectra, and scans we used are provided in data S1. Our pre- and post-sampling DTMs are provided as data S2 and S3 or can be accessed in the Small Body Mapping Tool (SBMT; <https://sbmt.jhuapl.edu>) by following the instructions in data S1. **License information:** Copyright © 2022 the authors, some rights reserved; exclusive licensee American Association for the Advancement of Science. No claim to original US government works. <https://www.science.org/about/science-licenses-journal-article-reuse>

SUPPLEMENTARY MATERIALS

science.org/doi/10.1126/science.abm1018

Materials and Methods

Supplementary Text

Figs. S1 to S26

Tables S1 to S7

References (52–90)

Movies S1 to S6

Data S1 to S3

Submitted 28 August 2021; accepted 10 June 2022

Published online 7 July 2022

10.1126/science.abm1018